CFD analysis of the HVAD's hemodynamic performance and blood damage with insight into gap clearance

Antonio Gil[a]; Roberto Navarro[a]; Pedro Quintero[a]; Andrea Mares[a1];
Manuel Pérez[b]; Jose Anastasio Montero[b]

[a] CMT-Motores Térmicos, Universitat Politècnica de València, Camí de Vera, s/n, Valencia, 46022, Spain
[b] Servicio de Cirugía Cardíaca, Hospital Universitario La Fe, Avinguda de Fernando Abril Martorell, 106, Valencia, 46026, Spain

Abstract – Mechanical circulatory support using ventricular assist devices has become commonplace in the treatment of patients suffering from advanced stages of heart failure. While blood damage generated by these devices has been evaluated in depth, their hemodynamic performance has been investigated much less. This work presents the analysis of the complete operating map of a left ventricular assist device, in terms of pressure head, power and efficiency. Further investigation into its hemocompatibility is included as well. To achieve these objectives, computational fluid dynamics simulations of a centrifugal blood pump with a wide-blade impeller were performed. Several conditions were considered by varying the rotational speed and volumetric flow rate. Regarding the device's hemocompatibility, blood damage was evaluated by means of the hemolysis index. By relating the hemocompatibility of the device to its hemodynamic performance, the results have demonstrated that highest hemolysis occurs at low flow rates, corresponding to operating conditions of low efficiency. Both performance and hemocompatibility are affected by the gap clearance. An innovative investigation into the influence of this design parameter has yielded decreased efficiencies and increased hemolysis as the gap clearance is reduced. As a further novelty, pump operating maps were non-dimensionalized to highlight the influence of Reynolds number, which allows their application to any working condition. The pump's operating range places it in the transitional regime between laminar and turbulent, leading to enhanced efficiency for the highest Reynolds number.

Keywords – Centrifugal blood pump, Operating map, Non-dimensional analysis, Gap clearance, Shear stress, Hemolysis

Declarations – Not applicable.

Acknowledgements – This study was partially funded by UPV-La Fe through the innovation projects subprogram (reference MODELVAD).

[*] Corresponding author: anmabo4@etsid.upv.es (Mares, Andrea). ORCID: 0000-0002-3720-6710

1. INTRODUCTION

Cardiovascular diseases are one of the most frequent causes of death worldwide (World Health Organization 2014), with increasing prevalence in most developed countries (Mosterd and Hoes 2007). Despite the several available treatment options (Almenar et al. 2011), until recent decades patients afflicted by the most advanced stages of heart failure (HF) could not benefit from any medical therapy aside from transplants. However, availability of compatible heart donors is highly limited. Consequently, Mechanical Circulatory Support (MCS) using blood pumps has been developed as an alternative therapy that is being increasingly applied. First blood pumps consisted in extracorporeal circulation devices that provided temporary support, whereas more recent Ventricular Assist Devices (VADs) have made possible a longer-term and more comfortable assistance due to their smaller size (McKellar 2020).

VADs are mechanical blood pumps designed to assist or completely replace the function of left, right or both ventricles, in order to grant the required cardiac output (CO) when the heart itself is not able to provide it (Fraser et al. 2011). Left Ventricular Assist Devices (LVADs) aid in the pumping of the left ventricle (LV). Implanting blood pumps has become a standard therapy for patients suffering HF (Larose et al. 2010), as a bridge to transplant or to recovery (Stehlik et al. 2010) as well as a destination therapy (Kirklin et al. 2014), and nowadays it is the main treatment option when transplantation is not possible. Nevertheless, these devices are associated with complications that must be overcome, such as bleeding and stroke (Bluestein et al. 2010; Al-Quthami et al. 2012).

Two main aspects must be considered when designing and evaluating a VAD: hemodynamic performance and hemocompatibility. On the one hand, hemocompatibility is related to the blood damage caused by the device (Wiegmann et al. 2018) owing to non-physiological flow conditions such as device-induced turbulence (Avci et al. 2021). On the other hand, the performance of a hydraulic pump is evaluated by means of pressure head, power consumption and efficiency. These variables depend on the operating condition (rotational speed and flow rate), which justifies the importance of obtaining the entire operating map. The efficiency quantifies the hydraulic energy increment of the flow through the pump in percentage of the shaft power. Typical values of VAD's efficiency are in the range 20-30% (Fraser et al. 2011). Therefore, most of the consumed energy is not used to increase the pressure head of the flow. Increasing efficiency would imply a reduction in losses, as well as a prolongation of the battery life. Moreover, improving the hemodynamic performance to enhance the pump's efficiency constitutes a crucial task that will simultaneously improve the hemocompatibility of the device.

Numerous works have been published investigating different constant-flow devices based on axial and centrifugal rotary blood pumps. Nevertheless, while blood trauma is deeply investigated in every work regarding VADs, hardly any authors include an evaluation of the pump's hemodynamic performance through its complete operating map. Thamsen et al. (2015) analysed the blood damage generated within two LVADs: HeartMate II (axial) and HeartWare (centrifugal); and obtained similar hemolysis for both pumps, with the highest damage produced at the edges of blades and in the gap regions respectively. Zhang et al. (2020) analysed both normal and hypertension conditions in several pumps and obtained a 30% increase of hemolysis levels under the latter. Furthermore, a potentially higher risk of blood trauma operating at low-flow conditions is reported by several authors. Granegger et al. (2020) compared the hemocompatibility of HeartWare for adult (high-flow) and pediatric (low-flow) operating conditions, and discovered larger stagnation zones and residence times within the pump for the pediatric case, resulting in higher hemolysis. Thamsen et al. (2020) investigated the flow within the HeartMate III (centrifugal) under two flow conditions representing the lower (diastole) and upper (systole) physiologic flow range. Schöps et al. (2021) studied the blood trauma associated to an extracorporeal membrane oxigenation (ECMO) device under low- and high-flow operating conditions. Both obtained larger recirculation zones and more disturbed flow fields inside the pumps and, therefore, increased hemolysis for the low-flow condition. Although different operating conditions were considered in these works, the complete map was not obtained and the performance variables were not evaluated. The blood flow rate through the pump depends on patient's arterial pressure since it operates at a constant speed. Thus, studying its complete operating map, in terms of both hemodynamic performance and hemolysis, is of vital importance because it will work within a range of operating conditions. Wang et al. (2019) and Wu et al. (2021) presented the map of H-Q curves, which relates pressure head with operating conditions of a centrifugal device. However, it was only used for validation purposes, and the results of both studies focused on hemocompatibility. In this sense, the current work will contribute by analysing the complete operating map of a LVAD, even in terms of non-dimensional variables, and relating it to the device's hemocompatibility.

In this paper, blood flow within the Medtronic's continuous flow centrifugal pump HeartWare VAD (HVAD) is analysed. This pump employs a hybrid levitation system to position the impeller through the balance of magnetic and hydrodynamic forces. It has a 4-wide-blade impeller whose large top and bottom surfaces are tapered to produce hydrodynamic lift, while magnetic bearing is generated between center post's coils and impeller's magnets (Foster 2018). The hydrodynamic lift is speed dependent, leading to different gap clearances as the rotational speed changes. Hybrid and fully magnetic levitation bearings have replaced mechanical bearings to avoid friction, heating and dynamic sealing, which reduces blood damage risk (Wu et al. 2021). Nonetheless, HVAD was recently withdrawn from the market owing to elevated thrombogenicity. The aim of this work is to investigate in depth the HVAD's hemodynamics and to clarify the causes of its thrombotic complications. The thrombus begins to form with the chemical or mechanical activation of platelets, and then it grows in zones where activated platelets are prone to deposit. Note that activation and deposition might occur at different locations. Regions of the flow field characterized by high velocity gradients are exposed to elevated non-physiological shear stresses during certain exposure times, giving rise to potential risk of hemolysis and platelet mechanical activation (Wiegmann et al. 2019). Recirculation and stagnation regions, which involve large residence and exposure times, are prone to hemolysis, platelet deposition and thrombus growth. Elevated values of plasma free hemoglobin, caused by hemolysis, also promote the coagulation cascade (Bartoli et al. 2018). Considering these relations, thrombosis will be qualitatively related to the velocity and hemolysis fields. In this work, both hemodynamic and hemolytic performance will be related to shear stresses produced within gaps, and the influence of gap clearance will be discussed as a novel contribution to the knowledge about the HVAD. Furthermore, the non-dimensional analysis of operating maps will help in understanding the device's performance.

2. MATERIALS AND METHODS

2.1 Computational modeling

2.1.1 Solver and governing equations

Computational Fluid Dynamics simulations are performed to evaluate the flow within the HVAD, using the software SimCenter STAR-CCM+ (Siemens). The blood is modeled as a liquid with density $\rho = 1060\,\mathrm{kg/m^3}$ and assumed to be a Newtonian fluid, i.e. with constant viscosity $\mu = 3.5\,\mathrm{mPa}\cdot s$, since its non-Newtonian behavior is expected to be negligible at shear rates $\dot{\gamma} > 100\,s^{-1}$ such as those found in VADs (Fraser et al. 2011; Wiegmann et al. 2018, 2019; Wang et al. 2019). There are zones within the pump, however, where this assumption does not apply owing to lower shear rates. Consequently, additional computations have been performed to ensure applicability of this assumption, resulting in acceptable discrepancies: relative errors were below 1% for all the performance variables, except at the low-flow condition which resulted in errors of 6% and 9% for pressure head and efficiency respectively.

Given a working fluid, the fluid dynamics features within the device are entirely defined by the rotational speed of the impeller (Ω) and volumetric flow rate (Q). Several operating conditions are considered by varying these parameters in range of $[1800{,}4000]\ \mathrm{rpm}$ and $[1{,}10]\ \mathrm{L/min}$ respectively. The flow field through the pump is not affected by the mean pressure since the working fluid is incompressible. Therefore, the reference stagnation pressure of $p_t = 760\ \mathrm{mmHg}$ is imposed at the inlet. Mass flow equal to $\dot{m} = \rho\, Q$ at the outlet and no-slip walls are imposed as further boundary conditions.

The simulations are performed using both steady and transient approaches. For the steady-state simulations, the impeller motion is imposed by means of a Moving Reference Frame (MRF) approach. It consists in formulating the set of equations for the rotating region in a reference frame that moves with the angular velocity of the impeller, neglecting transient effects and allowing its solution in a steady-state simulation. This is achieved by including an additional term of inertial forces in the momentum equation. The MRF approach is employed together with a mixing plane interface between rotating and static regions to avoid circumferential heterogeneity due to the frozen impeller (Galindo et al. 2020). For the unsteady-state simulations, the motion is reproduced using a sliding mesh approach and time is discretized employing a second order approach. The time-step is chosen corresponding to 0.5 deg of rotation with 10 inner iterations per step. This time-step leads to convective Courant numbers $CFL < 1$ in 96% of the fluid volume. Up to ten revolutions are needed to achieve a cyclic solution. Time-averaged values of the performance variables are obtained from the last revolution for the analysis.

Reynolds-Averaged Navier-Stokes (RANS) and Unsteady RANS (U-RANS) equations are solved to obtain the mean flow solution, in steady and transient approaches respectively. These equations are derived from the complete set of mass, momentum and energy conservation equations by imposing the Reynolds decomposition. The mass and momentum equations for the mean flow are solved assuming incompressible flow, while the energy equation is not needed. These equations can be found in Pope (2001). The momentum equation incorporates a source term of inertial and body forces which corresponds to the additional term included by the MRF approach, calculated as described by Torregrosa et al. (2019).

To achieve closure of RANS and U-RANS equations, the Reynolds stresses must be estimated using an appropriate turbulence model. Several turbulence models have been compared, resulting in differences below 3% on the performance variables. The k-ω model with shear stress transport (SST), proposed by Menter (1993), is selected, which is employed by most authors (Gross-Hardt et al. 2019) and is considered the standard model for turbomachinery applications. This turbulence model solves two additional transport equations and, hence, requires the imposition of two turbulence boundary conditions. The turbulence intensity and turbulent length scale at the inlet are set to be $I_t = 0.01$ and $L_t = 0.001\ \mathrm{m}$, respectively. The effect of these parameters over the solution has been investigated and found to be negligible.

2.1.2 Geometry, fluid domain and mesh

A CAD model of the HVAD was obtained by 3D-scanning using a HDI Advance 3D scanner, which employs structured-light technology and delivers high-resolution digital scans with an accuracy of 50 μm. The resulting fluid domain is presented in Fig. 1 (a), showing the wide-blade impeller. Its main dimensions are listed in Table 1. Since gap clearance depends on rotational speed, a parametric study is done varying its value within the range specified in Table 1. The top clearance is imposed by translating the impeller along the shaft axis. The resulting values of bottom gap clearance are not presented in Table 1 because it has a significant radial variation due to this surface's taper angle, moreover its effect is found to be negligible compared to that of the top gap clearance. The geometry with a top clearance of 40 µm is considered the main configuration, based on the order of magnitude used in the literature and shown in Table 2.

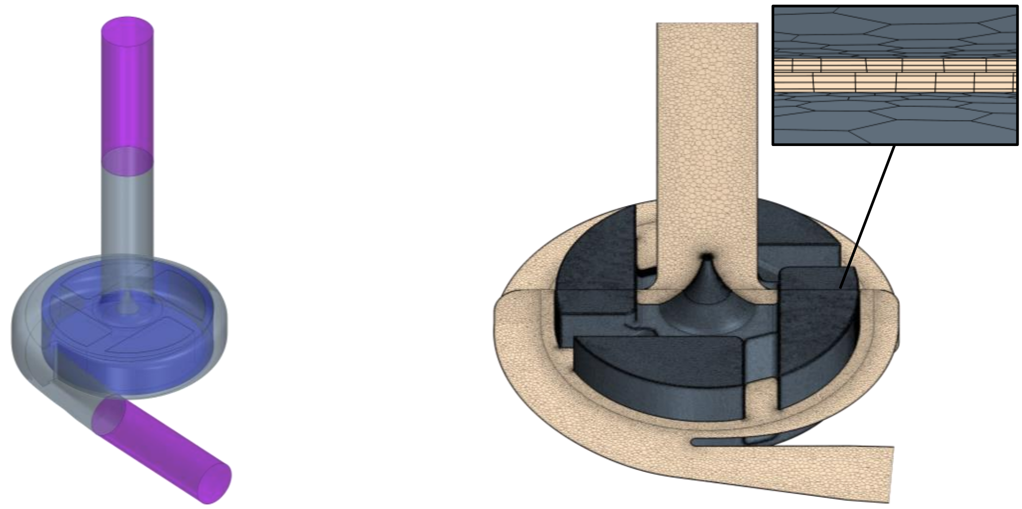

(a) **(b)**

Fig. 1 Computational domain and mesh of the HVAD. **(a)** Fluid domain: static region (gray), rotating region (blue) and inlet/outlet cannulas (violet, not to scale); **(b)** Sketch of the mesh, including a zoom of the thin mesh in the gap region

Parameter	Symbol	Value	Units
Impeller diameter	D_{imp}	34.6	mm
Inlet diameter	D_{inlet}	12.75	mm
Outlet diameter	D_{outlet}	10	mm
Channel width	w	3.8	mm
Top gap clearance	c	$[20{,}60]$	$\mu\mathrm{m}$

Table 1 Main dimensions of the HVAD and values of top gap clearance

Reference	Gap clearance
Chen et al. (2019)	$40\ \mu\mathrm{m}$
Thamsen et al. (2015)	$40\ \mu\mathrm{m}$
Granegger et al. (2020)	$[20, 23]\ \mu\mathrm{m}$
Foster (2018)	$[40, 70]\ \mu\mathrm{m}$

Table 2 Values of top gap clearance stated by other authors (Thamsen et al. 2015; Foster 2018; Chen et al. 2019; Granegger et al. 2020)

Polyhedral grids are generated to discretize the fluid volume. A polyhedral mesh is chosen since it ensures grid independence with fewer elements compared to tetrahedral meshes (Spiegel et al. 2011). The mesh includes a 10-element prism boundary layer along the walls, as well as local refinements in the rotating region and around the center post. A mesh independence study is performed for each configuration. Results of the mesh study for the main configuration are shown in Fig. 2 and summarized in Table 3, and analogous results are obtained for the configurations with clearances of 20 and 60 μm. The mesh reference size is taken to be $8 \cdot 10^{-4}$ m with refinement sizes of around $1 \cdot 10^{-4}$ m in the rotating region, leading to a mesh of 9.5×10^{6} volume cells (medium mesh), represented in Fig. 1 (b). Since a turbulence model (k-ω SST) is used, the quality of the boundary layer's mesh is evaluated by means of the wall $y^{+} = \frac{u_{\tau} y}{\nu}$ (Pope 2001). Reynolds number is relatively low at every operating condition, hence y^{+} must be less than 1 to ensure an accurate prediction of turbulence across the boundary layer. All grids have $y^{+} < 1$ in most part of the walls, guaranteeing a correct modeling of the viscous sublayer. Specifically, the portion of wall areas with $y^{+} > 1$ is 6% for the main configuration. Inlet and outlet cannulas with a longitude of 14-diameters are added in order to allocate the boundary conditions sufficiently far from the zone of interest. Note that this domain including long inlet and outlet ducts is not representative of the HVAD inserted in the heart apex, but similar to the experimental test bench configuration.

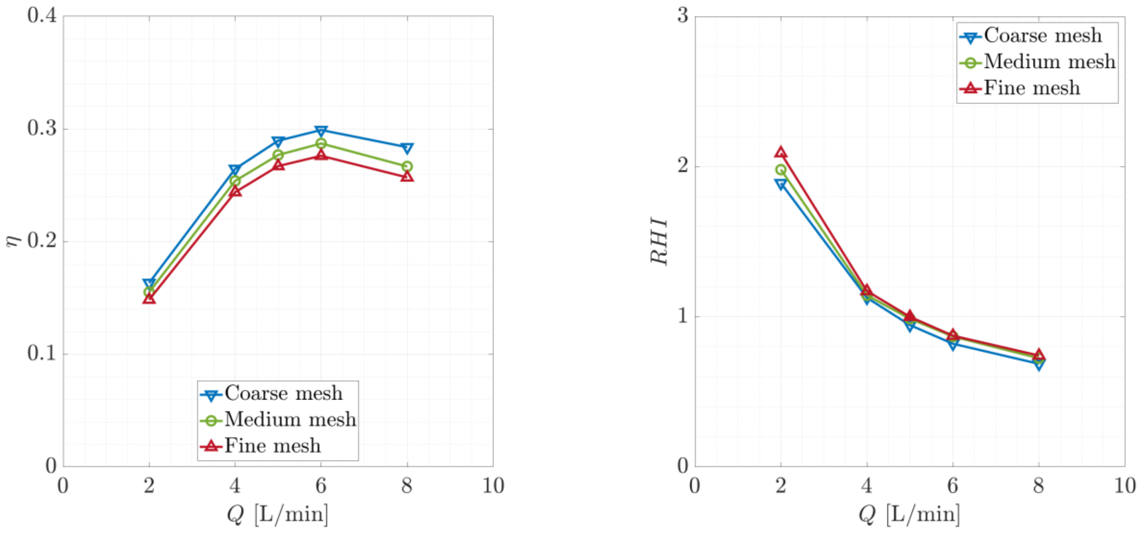

(a) **(b)**

Fig. 2 Results of the mesh independence study for the HVAD's main configuration (40μm-clearance gap) operating at Ω = 3000 rpm: **(a)** Efficiency; **(b)** Relative hemolysis index, taking the hemolysis index obtained using the fine mesh and operating at Q = 5 L/min as the nominal hemolysis index

	Coarse mesh	Medium mesh	Fine mesh
Reference size	$1.6 \cdot 10^{-3}$ m	$8 \cdot 10^{-4}$ m	$4 \cdot 10^{-4}$ m
Number of cells	2.7×10^{6}	9.5×10^{6}	33×10^{6}
Mean relative error: Δp_t	4.8 %	2.2 %	–
Mean relative error: η	9.1 %	4.0 %	–
Mean relative error: HI	6.5 %	2.4 %	–

Table 3 Mesh settings and results for coarse, medium, and fine grids

2.1.3 Blood damage and hemolysis calculation

Despite the increasing use of VADs in HF patients, several device-induced complications remain (Bluestein et al. 2010). As a device's size is reduced, gap widths decrease and impeller speeds increase, and, consequently, flow-induced blood damage becomes a more significant issue (Fraser et al. 2011). This damage is directly related with the scalar shear stress (SSS) level, defined in Equation 1 where σ_{ij} are the viscous stress components and u_i denotes the ith component of velocity. Note that SSS depends on both shear (σ_{ij}) and normal (σ_{ii}) components of stress. The Reynolds stress components are not considered for SSS calculation since Reynolds stress tensor is a statistical quantification of the averaged transport of fluctuating momentum, and has no direct link to physical forces acting over blood cells (Ge et al. 2008).

$$SSS = \tau = \sqrt{\frac{1}{6}\sum_{i \neq j}\left(\sigma_{ii} - \sigma_{jj}\right)^2 + \sum_{i \neq j}{\sigma_{ij}}^2} \qquad 1$$

$$\sigma_{ij} = \mu\left(\frac{\partial u_i}{\partial x_j} + \frac{\partial u_j}{\partial x_i}\right)$$

Hemolysis consists in the disintegration of red blood cells (RBCs) resulting in a release of hemoglobin into the blood plasma. It is related to the flow-induced mechanical damage to RBCs, and is normally more investigated than damage to other blood components (Bluestein et al. 2010). Diverse methods have been proposed for calculating the hemolysis index (HI). Most of them are power law models due to their simplicity and applicability to a wide range of devices (Taskin et al. 2012). Equation 2 shows the expression of the power law, that relates HI with SSS (τ) and exposure time (t). The HI is defined as the ratio of hemoglobin released into the blood plasma (Δhb) to total blood hemoglobin concentration, assumed to be $HB = 10\ \mathrm{g/dL}$ (Chen et al. 2019).

$$HI = \frac{\Delta hb}{HB} = C \cdot t^{\alpha} \cdot \tau^{\beta} \qquad 2$$

Based on Equations 1 and 2, an accurate velocity field is needed to obtain a reliable prediction of HI (Karimi et al. 2021). On the other hand, the non-linearity of Equation 2 implies that the HI at the domain outlet cannot be calculated as the sum of local values of HI based on the scalar shear stress and the residence time of RBCs in each grid cell (Wu et al. 2021). Thus, estimating the exposure time to a given shear stress level becomes complicated since it is not equivalent to the residence time. Taskin et al. (2012) made an evaluation of different power law models, for both Eulerian and Lagrangian approaches, and stated that available methods could not predict an accurate value of HI, but they were useful in predicting relative hemolysis for comparative purposes. For the Eulerian approach, a passive scalar transport equation must be solved. Garon and Farinas (2004) and Farinas et al. (2006) demonstrated the conversion from the non-linear Equation 2 to an expression linearized in time that can be easily derived to formulate the transport equation. This conversion allows the evaluation of HI in the whole domain, avoiding the exposure time estimation. Moreover, an Eulerian approach is preferred since it considers all areas contributing to the hemolysis, whereas some regions could be omitted using Lagrangian methods based on streamlines. The scalar transport equation considered in this work is presented in Equation 3, where the passive scalar is $\Delta hb' = \Delta hb^{1/\alpha}$. Note that the diffusion term is excluded.

$$\frac{\partial(\Delta hb')}{\partial t} + u_j \cdot \frac{\partial(\Delta hb')}{\partial x_j} = \left(HB \cdot C \cdot \tau^{\beta}\right)^{\frac{1}{\alpha}} \qquad 3$$

The right-hand side of Equation 3 represents the scalar source term. The values for the empirical constants are set to be $\mathrm{C} = 1.8 \times 10^{-6}\mathrm{s}^{-\alpha}\mathrm{Pa}^{-\beta}$, $\alpha = 0.765$ and $\beta = 1.991$, obtained by regressing experimental data from Heuser and Opitz (1980) (Song et al. 2003), since these values allow the application of the power law to wider ranges of shear stress (Taskin et al. 2012). This transport equation is solved, assuming $HI = 0$ at the inlet. The device's HI is evaluated as the mass-flow-average of this parameter at the outlet, as defined in Equation 4 (Craven et al. 2019).

$$HI_{device} = \frac{\oint_{outlet} HI\ |\mathbf{u} \cdot d\mathbf{A}|}{\oint_{outlet} |\mathbf{u} \cdot d\mathbf{A}|} \qquad 4$$

Since HI models do not predict an accurate absolute value, the relative hemolysis is evaluated by means of the relative hemolysis index (RHI), calculated as in Equation 5 assuming $\{\Omega = 3000\ \mathrm{rpm}, Q = 5\ \mathrm{L/min}\}$ as the nominal operating condition.

$$RHI = \frac{HI}{HI_{nominal}} \qquad 5$$

2.2 Experimental testing

The HVAD's operating map is obtained experimentally in order to validate the CFD results in terms of pressure head. The device is tested in a closed loop operating at different rotational speeds and adjusting the flow rate with a needle valve. The pressure head is measured using two high-quality pressure transmitters (WIKA PE 81.61 S-20, [0,1600] bar, WIKA Instruments, Germany) allocated at around 5 cm from the device's inlet and outlet. A radial flow turbine flowmeter (RS PRO 257-133, [1.5,30] L/min, RS Components, UK) is connected downstream of the pump's outlet, at a distance of 15 cm, to measure the flow rate. A distilled water–glycerol mixture (40% of glycerin) is used to simulate the blood viscosity of $\mu = 3.5\ \mathrm{mPa \cdot s}$. The experimental test bench is shown in Fig. 3 together with a sketch of the flow loop.

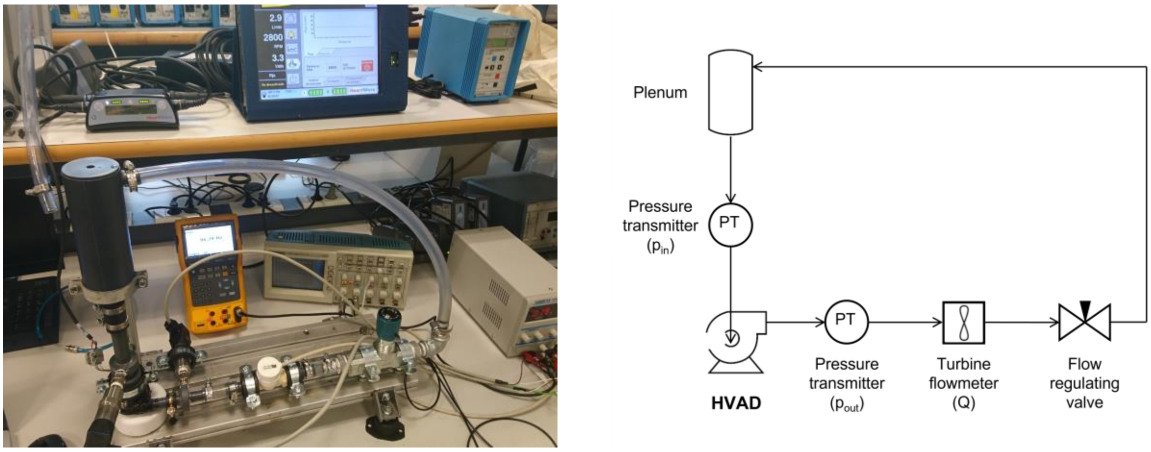

(a) **(b)**

Fig. 3 Experimental set-up: **(a)** Photography of the test bench showing a plenum upstream of the pump, inlet and outlet pressure sensors, the flowmeter, a flow regulating valve and the HVAD's controller and monitor; **(b)** Sketch of the flow loop

3. RESULTS AND DISCUSSION

3.1 Validation of the model

Fig. 4 shows the pump's pressure head (Δp_t) against the volumetric flow rate for three values of rotational speed, comparing the results from CFD steady-state simulations to the experimental measurements. An acceptable degree of discrepancies is achieved since the maximum relative error is less than 5% of the calculated value. Note that the device's pressure head is validated solely, whereas experimental validation for the mechanical shaft power and for the HI have not been performed.

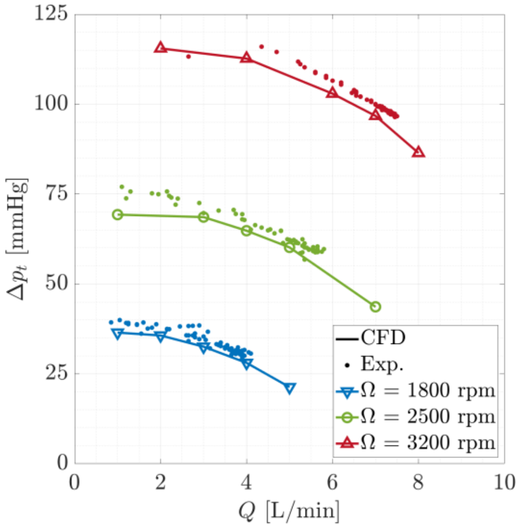

Fig. 4 Pressure head against volumetric flow rate for several values of rotational speed: curves obtained numerically compared to points measured experimentally

Additionally, the pump's operating maps obtained in steady and transient approaches are compared. The time-averaged values during the last revolution are considered for the transient approach.

The pressure head map is represented in Fig. 5 (a) for both steady- and unsteady-state simulations. Despite differences found at low and high flow rates with maximum relative errors of 6% and 10% respectively, the steady approach agrees reasonably well with transient results, principally at nominal operating conditions.

The efficiency (η) is defined as the hydraulic energy increment of the flow through the pump ($\Delta\dot{E}$) in percentage of the mechanical shaft power (P), as shown in Equation 6 where T represents the torque acting on the impeller.

$$\eta = \frac{\Delta\dot{E}}{P} = \frac{Q\Delta p_t}{\Omega T} \qquad 6$$

The pump's efficiency map is represented in Fig. 5 (b) for both approaches, showing discrepancies even at nominal operating conditions, with a 10% of maximum relative error between steady and transient predictions.

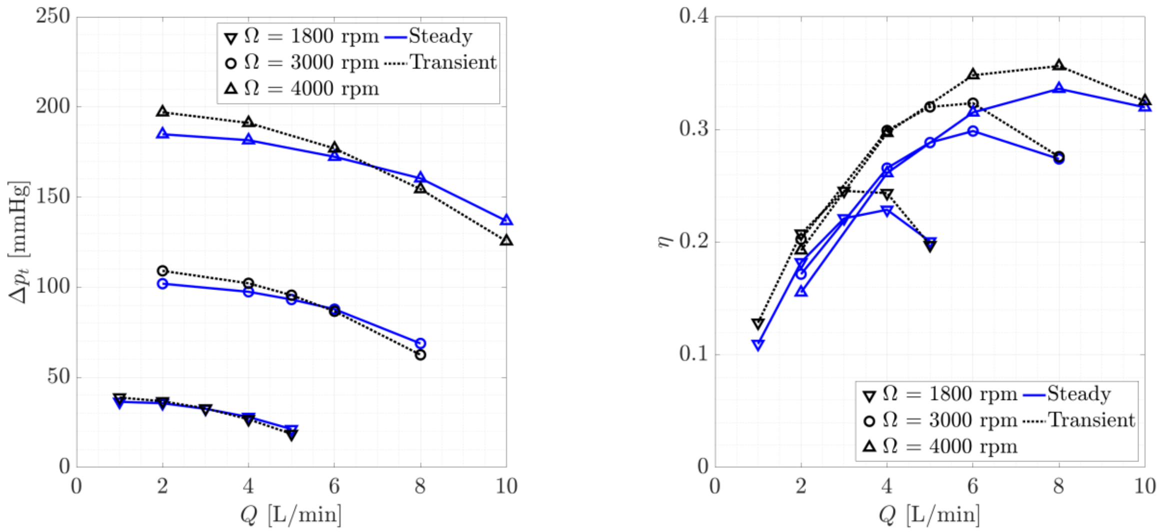

(a) **(b)**

Fig. 5 Performance variables against volumetric flow rate for several values of rotational speed: comparison between steady and transient approaches. **(a)** Pressure head; **(b)** Efficiency

The device's RHI curve, operating at $\Omega = 3000$ rpm, is represented in Fig. 6 for both steady and transient approaches, and a constant relative error of 10% is obtained.

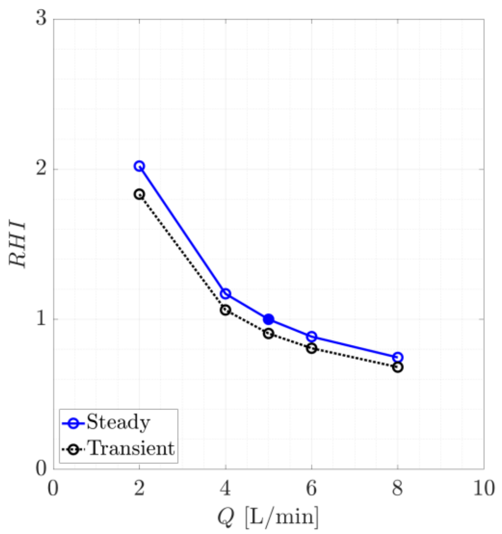

Fig. 6 Relative hemolysis index against volumetric flow rate, operating at Ω = 3000 rpm: comparison between steady and transient approaches, taking the hemolysis index obtained using the steady approach and operating at Q = 5 L/min as the nominal hemolysis index

Based on the experimental validation, the CFD model predicts the HVAD's performance with enough accuracy. Despite discrepancies found between steady and transient approaches, the steady MRF approach is used for the evaluation of the following sections, owing to its considerably lower computational cost. All the simulations were performed on an Intel® Xeon® Gold 6248R CPU, using 48 parallel processes. Computational times were 8.7 s per iteration and 163.2 s per time-step in steady- and unsteady-state simulations respectively, resulting in 2 to 6 hours of calculation for the steady approach, and around 330 hours of calculation for the transient approach.

3.2 Pump's operating map

The hemodynamic performance of the HVAD is evaluated, for the main configuration (40µm-clearance gap), by means of its operating maps. The pressure head and the shaft power, against the volumetric flow rate, are represented in Fig. 7 for different rotational speeds: $\Omega = 1800\ \mathrm{rpm}$ and $\Omega = 4000\ \mathrm{rpm}$ are the minimum and maximum speeds respectively, while $\Omega \in [2400, 3200]\ \mathrm{rpm}$ represents the pump's normal operating range. The pressure head equals the difference between afterload (aortic pressure) and preload (LV pressure). The mean arterial pressure (MAP) is the temporal mean of the aortic pressure during one cardiac cycle. Hence, the appropriate pressure head is determined by subtracting the LV pressure to the patient's MAP. Although the LV pressure is fluctuating, it can be assumed to be constant and equal to the LV end-diastolic pressure, $p_{LV} \approx 14\ \mathrm{mmHg}$ (Jain et al. 2019), since the failing heart is hardly pumping. The desired flow rate, for its part, is given by the required CO. For a healthy adult weighing 70 kg, normal values of CO and MAP at rest are $\mathrm{CO} \approx 5\ \mathrm{L/min}$ and $\mathrm{MAP} \in [70, 100]\ \mathrm{mmHg}$. Based on Fig. 7 (a), known as H-Q curves, these values establish the normal operation range for rotational speed within $\Omega \in [2400, 3200]\ \mathrm{rpm}$, as indicated previously. These H-Q curves follow the typical tendency for centrifugal pumps.

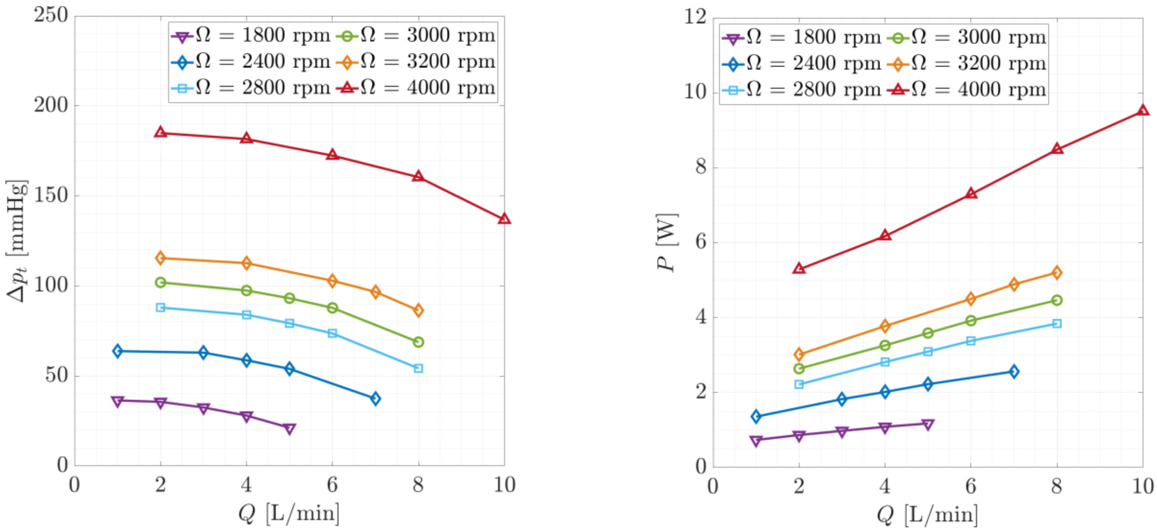

(a) **(b)**

Fig. 7 Performance variables against volumetric flow rate for several values of rotational speed, for the configuration with 40μm-clearance gap, and blood with normal hematocrit (μ = 3.5 mPa·s) as working fluid. **(a)** Pressure head; **(b)** Shaft power

An optimal volumetric flow rate exists for each rotational speed. This optimum involves a trade-off between sufficiently high increment of the flow energy, proportional to the pressure head, and low power consumption, and it is determined based on the efficiency map presented in Fig. 8.

Once implanted, the pump will operate at a constant rotational speed adjusted by the physician, whose value must be determined to produce the desired CO for normal values of MAP. Nevertheless, since arterial pressure can change, the flow rate will vary as the rotational speed is not readjusted in real time. Therefore, the device will eventually work at off-design conditions.

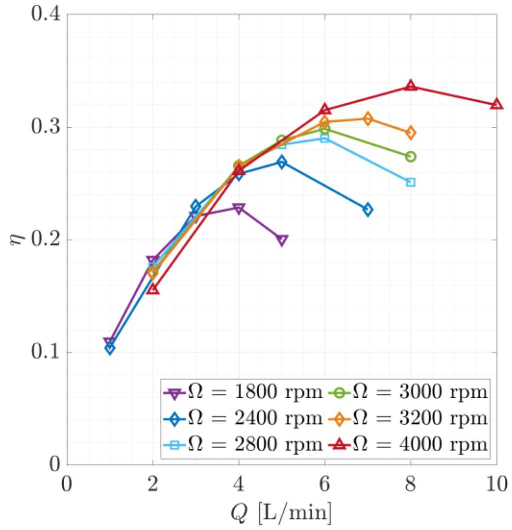

Fig. 8 Efficiency against volumetric flow rate for several values of rotational speed, for the configuration with 40μm-clearance gap, and blood with normal hematocrit (μ = 3.5 mPa·s) as working fluid

To analyze flow patterns involving recirculating and stagnant flow, the velocity field must be represented in an appropriate reference frame, i.e. relative to moving walls in the rotating region and relative to static walls in the static region. Thus, the relative velocity in the rotating region is the result of subtracting the rotating motion of this region to the absolute velocity. The relative velocity field within the pump is presented in Fig. 9 (a,b) for two different operating conditions at $\Omega = 3000\,\mathrm{rpm}$: $Q = 5\,\mathrm{L/min}$ (required CO for an adult) is a nominal condition near the optimal flow rate ($Q = 6\,\mathrm{L/min}$), while $Q = 2\,\mathrm{L/min}$ represents a point of excessively low flow rate. Recirculation zones are observed in the impeller channels for both operating conditions, indicating that an improved shape of the blades will lead to a more optimal design. An enlargement of those recirculation zones is detected for the low-flow case, as observed by other authors (Granegger et al. 2020; Thamsen et al. 2020; Schöps et al. 2021). As the flow rate increases, additional recirculation zones appear in the external wall of the impeller, at the adjacent blade of each channel. Note that the discontinuity in the velocity field at the interface between rotating and static regions is due to the change from moving to stationary reference frames (Karimi et al. 2021).

Flow patterns involving regions of recirculating and stagnant flow are, among other phenomena, responsible for thrombus formation within the device (Fraser et al. 2011). Zones with significant velocity gradients, as the impeller channels, are exposed to high shear stresses promoting platelet activation. Furthermore, within recirculating flow regions the blood's residence time is elevated promoting platelet deposition. Fig. 9 (c) shows an explanted HVAD where several thrombi have formed within the channels as well as around the impeller, where platelets were prone to deposit and form a clot due to flow recirculation seen in Fig. 9 (a,b). The photography in Fig. 9 (c) illustrates an advanced state of the thrombus formation reached after several months of operation, whereas the relative velocity field observed in Fig. 9 (b) corresponds to the initial state of the pump without clots. Note that, as activated platelets deposit in regions of low velocity and low shear stress (recirculation regions) forming the clot, the blood flow interacts with the growing thrombus leading to different fluid patterns. Therefore, the clot formation would have initiated in the recirculation regions observed in Fig. 9 (b). Then the clot, as it grows, would promote new recirculation regions where platelets continue to deposit enlarging the clot until the final thrombotic state shown in Fig. 9 (c) is reached. This HVAD was explanted from a patient who experienced complications due to blood clotting inside the pump. The explant was done before the composition of this article and the photography was taken just after the explant.

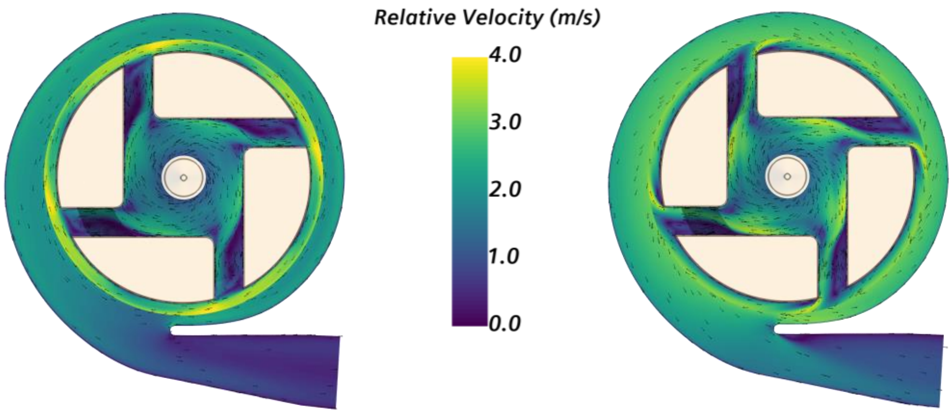

(a) **(b)**

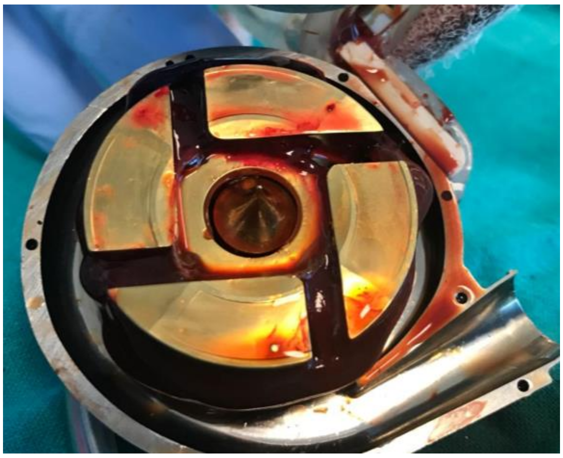

(c)

Fig. 9 Contours of the relative velocity field within the HVAD, for the configuration with 40μm-clearance gap operating at Ω = 3000 rpm and for blood with normal hematocrit (μ = 3.5 mPa·s) as working fluid: **(a)** Low-flow condition (Q = 2 L/min), **(b)** Nominal condition (Q = 5 L/min); **(c)** photography of an explanted HVAD showing the zones prone to thrombus formation, taken by the cardiac surgery team of Hospital La Fe

3.3 Gap clearance influence

One relevant design parameter of the HVAD is the gap clearance between impeller and housing. The influence of this parameter is evaluated, as a novelty for this device, since it is speed dependent and different gap clearances are used in the literature. Fig. 10 depicts the performance curves at $\Omega = 3000\,\mathrm{rpm}$ for the considered configurations.

It could be expected that small gaps are preferable since they lead to higher efficiencies because of the reduction in tip leakage (Fraser et al. 2011). Wiegmann et al. (2018) investigated the effect of design parameters on efficiency and blood damage for a centrifugal pump with conventional blades, and discussed the conflicting requirements for gap clearance: while large gaps reduce the maximum shear stress magnitude, small gaps induce less flow disturbances and provide higher efficiency. Hence, small gaps are expected to be preferable to maximize the hydraulic efficiency while large gaps lead to improved hemocompatibility. However, this device manifests the opposite tendency for efficiency: it decreases as the gap clearance is reduced. This decrease in efficiency can be justified by observing Fig. 10 (a,b): the pressure head is not affected while the consumed power increases. The increase in power can be explained based on Fig. 10 (d), where both pressure and shear power are represented. The pressure and shear components of the power are related to the torque exerted by the fluid on the impeller's walls, which consists of the moment due to the static pressure on the surface and the moment resulting from the shear stresses acting on it. While the shear power remains relatively constant, the magnitude of pressure power increases with flow rate. The shear power experiences a significant increase when halving the gap clearance since the secondary flow is generating higher shear stresses in the gap regions. The effect of gap clearance on pressure power, for its part, is negligible. Therefore, the shear component of the torque entails the main contribution to the reduction of efficiency when reducing the gap clearance. Moreover, the shear power is of the same order of magnitude than the pressure power, while it is normally few orders of magnitude lower in conventional turbopumps.

The wide-blade impeller and the extremely narrow gaps of the HVAD are thought to be originating this increase in shear torque, since these blades are notably thicker than conventional blades used in turbomachinery and gap clearances are orders of magnitude lower than those found in other pumps. While the efficiency decreases as gap clearance increases due to tip leakage in conventional pumps, this device has manifested the opposite effect. Potentially higher shear torque acts on the HVAD's impeller owing to two design characteristics: the extremely low value of gap clearance and the large blade tip areas involved in the gap region. This leads to reduced efficiencies as the gap clearance decreases. Nonetheless, efficiency does not increase monotonously with gap clearance, but will eventually decrease for larger clearances owing to the increase in tip leakage that leads to a significant decrease in pressure head. Nevertheless, larger values of gap clearance are not included in this study because the HVAD's design does not allow for such large clearances due to the requirements for hydrodynamic lift.

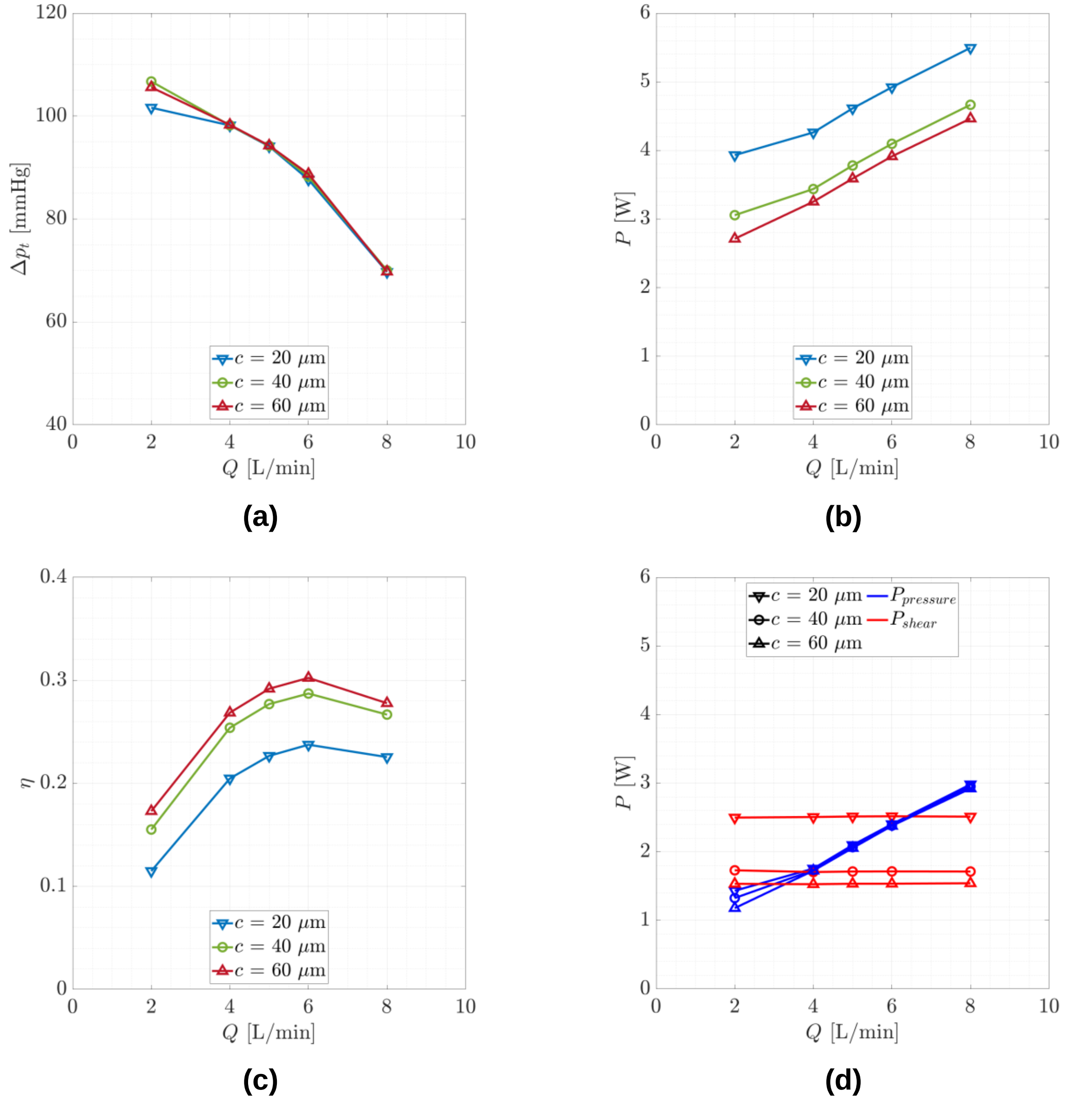

Fig. 10 Performance variables against volumetric flow rate, operating at Ω = 3000 rpm, for blood with normal hematocrit (μ = 3.5 mPa·s) as working fluid, and several values of gap clearance: **(a)** Pressure head; **(b)** Shaft power; **(c)** Efficiency; **(d)** Pressure and shear power

3.4 Blood damage: hemolysis

As described earlier, the hemolysis is investigated by means of the RHI defined in Equation 5. RHI against the volumetric flow rate is represented in Fig. 11 for several values of rotational speed (a) and gap clearance (b).

Fig. 11 (a) depicts that both increasing Ω and decreasing Q lead to an increase in HI, showing a similar trend as that obtained by Karimi et al. (2021). Increasing speeds produce more elevated shear stresses and, thus, higher hemolysis. Keeping constant the rotational speed, an asymptotic tendency is observed at high flow rates while an important increment of the risk of hemolysis is detected at low flow rates, as found by Thamsen et al. (2020), Granegger et al. (2020) and Schöps et al. (2021), due to longer washout times within the pump and larger zones of flow recirculation in the blade passages where the fluid is exposed to high velocity gradients and shear stresses.

According to the literature concerning other blood pumps, large gaps induce flow disturbances which increase shear stresses (Rezaienia et al. 2018), while narrow gaps induce cell screening in a way that, despite the higher maximum shear stress magnitude within the gap, less quantity of blood is exposed to those levels of shear stress since the secondary flow is reduced (Wiegmann et al. 2018). However, a global increase in the risk of hemolysis is detected in Fig. 11 (b) when reducing the gap clearance in the HVAD. Just as the decrease in efficiency, this increase in HI is a consequence of the increment of shear stresses over the large blade tip area involved in the gap region. Moreover, HVAD's gap clearances are extremely low, of the order of ten blood cells, each 6-8 μm in diameter, promoting elevated levels of hemolysis even for the larger gap considered in this work. For larger values of gap clearance, the HI will continue to decrease until the increment in secondary flow leads to a slight increase in hemolysis since more quantity of blood is exposed to elevated shear stress levels through gaps, but this increase is expected to be significantly lower than that observed for the values of gap clearance considered in this work and found in the HVAD.

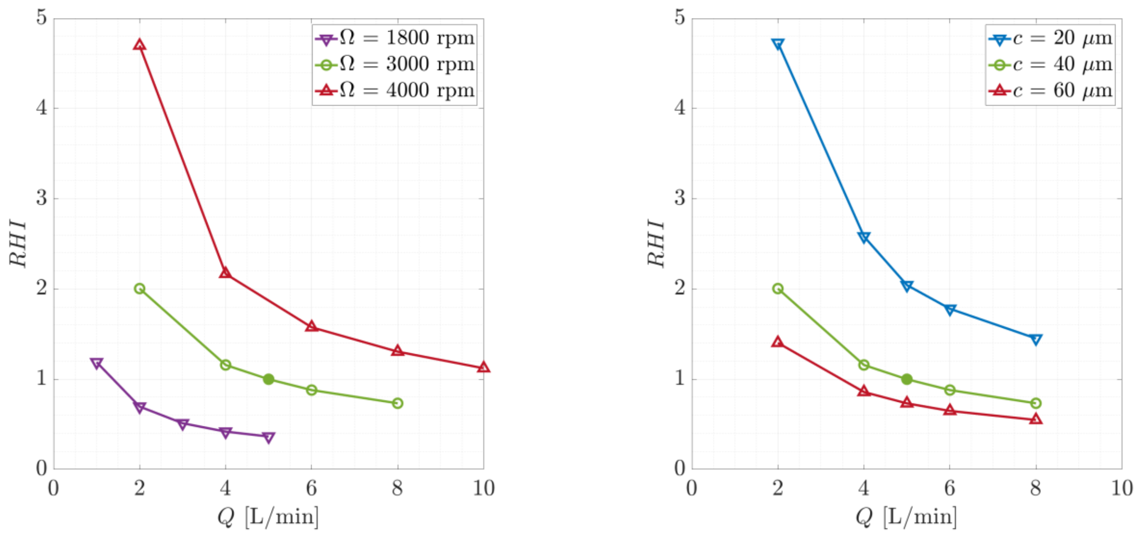

(a) (b)

Fig. 11 Relative hemolysis index against volumetric flow rate for several values of rotational speed and gap clearance, and blood with normal hematocrit (μ = 3.5 mPa·s) as working fluid**: (a)** Effect of rotational speed, for the configuration with 40μm-clearance gap; **(b)** Effect of gap clearance, operating at Ω = 3000 rpm

Fig. 12 depicts the HI field within the pump operating at $\Omega = 3000\ \mathrm{rpm}$ at low-flow and nominal conditions. The former presents globally higher HI than the latter, as detected in the literature (Granegger et al. 2020; Thamsen et al. 2020; Schöps et al. 2021) and discussed above. It can be seen how narrow gaps and recirculation zones induce a high degree of hemolysis, leading to increased HI downstream of the impeller.

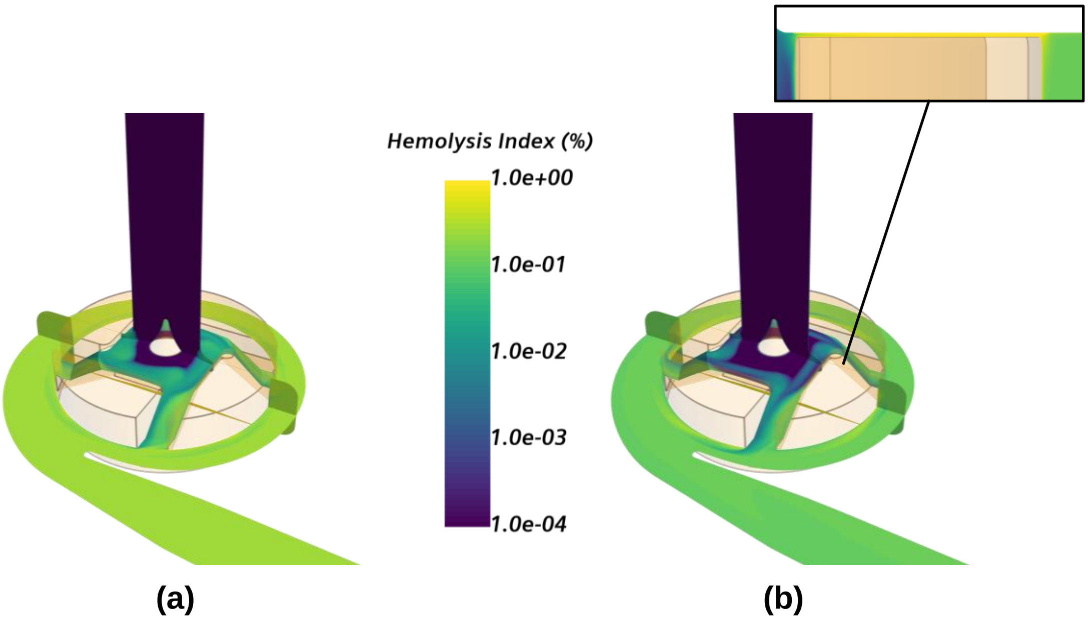

Fig. 12 Contours of the hemolysis index field within the HVAD, for the configuration with 40μm-clearance gap operating at *Ω* = 3000 rpm, and blood with normal hematocrit (*μ* = 3.5 mPa·s) as working fluid (gap zoom not to scale): **(a)** Low-flow condition (*Q* = 2 L/min); **(b)** Nominal condition (*Q* = 5 L/min)

3.5 Non-dimensional analysis

Previous figures can be extended to a non-dimensional form to ensure their applicability for multiple combinations of working conditions. Through a non-dimensional analysis it is observed that non-dimensional pressure head $\Delta p_t^* = \frac{\Delta p_t}{\rho \Omega^2 {D_{imp}}^2}$ and power $P^* = \frac{P}{\rho \Omega^3 {D_{imp}}^5}$ are a function of just the non-dimensional flow rate (flow number) $Q^* = \frac{Q}{\Omega {D_{imp}}^3}$ and the Reynolds number $Re = \frac{\rho \Omega {D_{imp}}^2}{\mu}$ (Heras 2011).

Note that increasing Reynolds numbers corresponds to increasing speeds or decreasing viscosities. The blood hematocrit indicates the quantity of RBCs present in the blood flow, which in turn affects the blood viscosity. The viscosity of $\mu = 3.5\ \mathrm{mPa} \cdot s$ corresponds to a hematocrit of 40% that is within the range of normal values of hematocrit for both men and women (Billett 1990). An increase in hematocrit produces an increment of the blood viscosity and, thus, a reduction of the Reynolds number.

Fig. 13 exhibits the non-dimensional operating maps, including two extreme conditions:

- Lowest Reynolds number: minimum speed ($\Omega = 1800\ \mathrm{rpm}$), extremely high hematocrit of 60% ($\mu = 8\ \mathrm{mPa \cdot s}$).
- Highest Reynolds number: maximum speed ($\Omega = 4000\ \mathrm{rpm}$), extremely low hematocrit of 20% ($\mu = 2\ \mathrm{mPa \cdot s}$).

Whilst the effect of Reynolds number over the non-dimensional pressure head can be assumed to be negligible for $Re \geq 10^5$, it is significant for the lowest Reynolds numbers, as detected in Fig. 13 (a). This phenomenon is explained through the critical Reynolds number marking the transition from laminar to turbulent flow, which is conventionally taken to be of the order 10^5 for rotor-based Re (Heras 2011). Above this value, Δp_t^* becomes Reynolds independent. Regarding the flow regime, Reynolds numbers are relatively low for blood pumps as compared to other hydraulic pumps, owing to their smaller size and the higher viscosity of the working fluid. Consequently, the operating conditions typical of blood pumps place them in the transitional regime between laminar and low Re turbulent regimes, where some degree of dependency on Reynolds number still exists (Smith et al. 2004).

The main contribution of the non-dimensional analysis is related to the operating map of P^*, shown in Fig. 13 (b). The HVAD's controller estimates the flow rate through the pump based on the supplied power. To do this, it consults several maps of $P(Q, \Omega)$, each corresponding to a different value of blood hematocrit. The non-dimensional map of $P^*(Q^*, Re)$ allows this estimation, for every value of hematocrit, without needing more than one map.

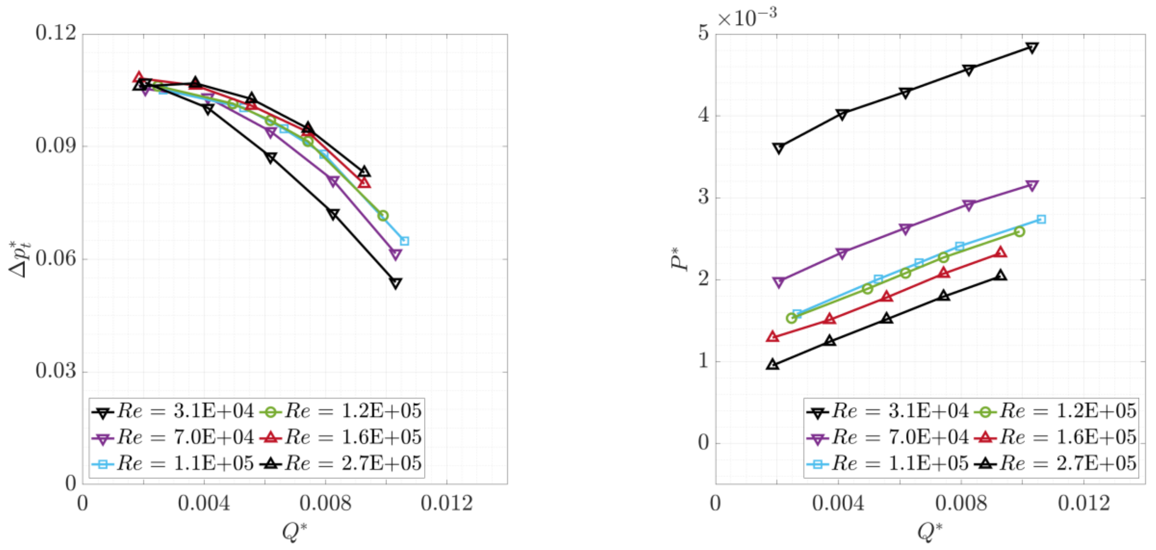

(a) **(b)**

Fig. 13 Non-dimensional performance variables against non-dimensional flow rate for several values of Reynolds number, for the configuration with 40μm-clearance gap: **(a)** Pressure head; **(b)** Shaft power. The different values of Reynolds number correspond to normal blood hematocrit (μ = 3.5 mPa·s) operating at four rotational speeds for the colored curves, and extremely low and high blood hematocrit (μ = 2 mPa·s and μ = 8 mPa·s) operating at the pump's maximum and minimum rotational speed, respectively, for the black curves

An important influence of Reynolds number is observed in Fig. 13 (b) for the non-dimensional power within the whole range, due to shear effects occurring in the gap region. Therefore, the different combinations of operating conditions do not collapse to the same efficiency curve in Fig. 14, where the optimal operating condition (Ω,Q) corresponds to $Q^* \approx 0.008$. A maximum pump efficiency of 10-40%, depending on Reynolds number, is obtained, which implies that most of the consumed energy is lost in form of vorticity and friction. This means that the mechanical energy supplied by the shaft is not just transformed into useful hydraulic energy provided to the flow, but also into lost energy consisting of friction losses due to the fluid's resistance to motion, related with the fluid's viscosity, and energy transferred to the recirculating flow and other turbulent features in form of vorticity. Friction losses explain the decrease in efficiency when augmenting the blood viscosity.

Although low viscosities would be preferable to maximize efficiency, low values of hematocrit involve complications regarding bleedings and insufficient clotting (Boneu and Fernandez 1987). Note, however, that this blood parameter depends on each patient and cannot be chosen.

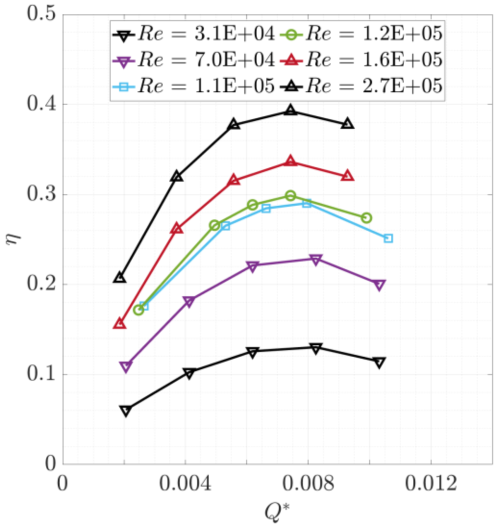

Fig. 14 Efficiency against non-dimensional flow rate for several values of Reynolds number, for the configuration with 40μm-clearance gap. The different values of Reynolds number correspond to normal blood hematocrit (μ = 3.5 mPa·s) operating at four rotational speeds for the colored curves, and extremely low and high blood hematocrit (μ = 2 mPa·s and μ = 8 mPa·s) operating at the pump's maximum and minimum rotational speed, respectively, for the black curves

4. CONCLUSIONS

This work has presented the complete operating maps for the HVAD in terms of pressure head, power and efficiency. The pressure head map (H-Q curves) reproduces the typical tendency for centrifugal pumps. The power map depicts an almost linear dependency on flow rate. An efficiency of around 30% is obtained at nominal conditions.

By relating the hemocompatibility of the HVAD to its hemodynamic performance, it has been demonstrated that the optimal combination of operating conditions corresponds to that of reduced blood damage. The influence of flow conditions on hemolysis has been investigated in a different manner, by means of the RHI map, leading to the same conclusion than other authors: the low-flow condition induces potentially higher risk of hemolysis due to longer residence times and larger zones of recirculating flow (Granegger et al. 2020; Thamsen et al. 2020; Schöps et al. 2021).

The study regarding the influence of gap clearance in the HVAD has manifested tendencies different than those expected for conventional turbopumps. Shear stresses within the narrow gap region act over large blade tip areas. Thus, potentially high shear torque acts on the wide-blade impeller, leading to reduced efficiencies and raised hemolysis as the gap clearance decreases. Furthermore, gap clearances in HVAD take values that correspond to the size of less than ten blood cells and, thus, leading to significantly high risk of RBC damage. As a contribution of this work, these narrow gaps, needed to produce hydrodynamic lift, are found to be significantly lower than the optimum value that would lead to maximum efficiency and minimum hemolysis. Hence, a fully magnetic levitation system would be preferable in comparison to the hybrid (hydrodynamic and magnetic) system used in the HVAD, since it would allow larger gap clearances.

In conclusion, the HVAD's complications that bring about its removal from the market can be attributed to its narrow gaps and to the shape of its wide-blade impeller, that lead to elevated shear stresses within gaps and flow recirculation zones in the blade passages of the impeller respectively, promoting both hemolysis and thrombosis. These observations will help in the design of a new device with enhanced hemocompatibility and improved hemodynamic performance.

Furthermore, the non-dimensional representation of operating maps has demonstrated that there is a significant influence of Reynolds number on performance variables within the normal range of operating conditions of these devices, especially on power and efficiency. This Reynolds dependency owes to the narrow gaps of the device, that produce elevated shear stresses over a large area of the wide-blade impeller. Moreover, the HVAD's controller estimates the flow rate based on the consumed power using several operating maps for different values of blood hematocrit. This estimation can be achieved using only one non-dimensional map containing performance data in terms of flow rate and power as a function of Reynolds number. Therefore, the non-dimensional representation of maps can imply a reduction in the data stored for the flow rate estimation performed by the controller.

The computational approach employed in this work has limitations. On the one hand, no experimental validation has been conducted for shaft power and hemolysis. On the other hand, several limitations regarding the numerical set-up must be mentioned. Firstly, the blood has been modeled as a Newtonian fluid, instead of considering its variable viscosity, but this is a valid assumption since shear rates within the device are greater than $100\ s^{-1}$ in most of the domain. Secondly, most studies of this work have been solved through steady-state simulations, dismissing transient effects. Nevertheless, some operating conditions have been calculated in unsteady-state simulations and acceptable differences have been found with respect to steady results, proving the validity of the MRF approach. Note that an important reduction of calculation time is achieved using this approach. Thirdly, the blood flow through the extremely narrow gaps of this device does not behave as a continuum. Since the hemolysis model employed in this work assumes that blood is a continuum, non-continuum effects within gaps have not been considered. Finally, some phenomena have not been evaluated, such us the effect of remaining native pulsatility and the consideration of realistic boundary conditions that model the LV volume at the inlet or the anastomosis to the aorta at the outlet.

5. REFERENCES

Al-Quthami AH, Jumean M, Kociol R, et al (2012) Eptifibatide for the treatment of Heartmate II left ventricular assist device thrombosis. Circ Hear Fail 5:68–70. https://doi.org/10.1161/CIRCHEARTFAILURE.112.966804

Almenar L, Díaz Molina B, Comín Colet J, Pérez De La Sota E (2011) Insuficiencia cardiaca y trasplante. Rev Esp Cardiol 64:42–49. https://doi.org/10.1016/S0300-8932(11)70006-9

Avci M, Heck M, O'Rear EA, Papavassiliou D V. (2021) Hemolysis estimation in turbulent flow for the FDA critical path initiative centrifugal blood pump. Biomech Model Mechanobiol. https://doi.org/10.1007/s10237-021-01471-3

Bartoli CR, Zhang D, Kang J, et al (2018) Clinical and In Vitro Evidence That Subclinical Hemolysis Contributes to LVAD Thrombosis. Ann Thorac Surg 105:807–814. https://doi.org/10.1016/j.athoracsur.2017.05.060

Billett HH (1990) Hemoglobin and Hematocrit. In: HK W, WD H, JW H (eds) Clinical Methods: The History, Physical, and Laboratory Examinations

Bluestein D, Chandran KB, Manning KB (2010) Towards non-thrombogenic performance of blood recirculating devices. Ann Biomed Eng 38:1236–1256. https://doi.org/10.1007/s10439-010-9905-9

Boneu B, Fernandez F (1987) The Role of the Hematocrit in Bleeding. Transfus Med Rev 1:182–185. https://doi.org/10.1016/S0887-7963(87)70020-0

Chen Z, Jena SK, Giridharan GA, et al (2019) Shear stress and blood trauma under constant and pulse-modulated speed CF-VAD operations: CFD analysis of the HVAD. Med Biol Eng Comput 57:807–818. https://doi.org/10.1007/s11517-018-1922-0

Craven BA, Aycock KI, Herbertson LH, Malinauskas RA (2019) A CFD-based Kriging surrogate modeling approach for predicting device-specific hemolysis power law coefficients in blood-contacting medical devices. Biomech Model Mechanobiol 18:1005–1030. https://doi.org/10.1007/s10237-019-01126-4

Farinas MI, Garon A, Lacasse D, N'dri D (2006) Asymptotically consistent numerical approximation of hemolysis. J Biomech Eng 128:688–696. https://doi.org/10.1115/1.2241663

Foster G (2018) Third-generation ventricular assist devices. Elsevier Inc.

Fraser KH, Taskin ME, Griffith BP, Wu ZJ (2011) The use of computational fluid dynamics in the development of ventricular assist devices. Med Eng Phys 33:263–280. https://doi.org/10.1016/j.medengphy.2010.10.014

Galindo J, Serrano JR, Navarro R, García-Olivas G (2020) Numerical modeling of centrifugal compressors with heterogeneous incoming flow due to low pressure exhaust gas recirculation. Turbomach Tech Conf Expo 1–13

Garon A, Farinas MI (2004) Fast three-dimensional numerical hemolysis approximation. Artif Organs 28:1016–1025. https://doi.org/10.1111/j.1525-1594.2004.00026.x

Ge L, Dasi LP, Sotiropoulos F, Yoganathan AP (2008) Characterization of hemodynamic forces induced by mechanical heart valves: Reynolds vs. viscous stresses. Ann Biomed Eng 36:276–297. https://doi.org/10.1007/s10439-007-9411-x

Granegger M, Thamsen B, Schlöglhofer T, et al (2020) Blood trauma potential of the

HeartWare ventricular assist device in pediatric patients. J Thorac Cardiovasc Surg 159:1519–1527. https://doi.org/10.1016/j.jtcvs.2019.06.084
Gross-Hardt S, Boehning F, Steinseifer U, et al (2019) Mesh sensitivity analysis for quantitative shear stress assessment in blood pumps using computational fluid dynamics. J Biomech Eng 141:. https://doi.org/10.1115/1.4042043
Heras S (2011) Fluidos, bombas e instalaciones hidráulicas
Heuser G, Opitz R (1980) A Couette viscometer for short time shearing of blood. Biorheology 17–24
Jain P, Shehab S, Muthiah K, et al (2019) Insights into Myocardial Oxygen Consumption, Energetics, and Efficiency under Left Ventricular Assist Device Support Using Noninvasive Pressure-Volume Loops. Circ Hear Fail 12:1–12. https://doi.org/10.1161/CIRCHEARTFAILURE.119.006191
Karimi MS, Razzaghi P, Raisee M, et al (2021) Stochastic simulation of the FDA centrifugal blood pump benchmark. Biomech Model Mechanobiol. https://doi.org/10.1007/s10237-021-01482-0
Kirklin JK, Naftel DC, Pagani FD, et al (2014) Sixth INTERMACS annual report: a 10,000-patient database. J Hear Lung Transplant 33:555–564. https://doi.org/10.1016/j.healun.2014.04.010
Larose JA, Tamez D, Ashenuga M, Reyes C (2010) Design concepts and principle of operation of the HeartWare ventricular assist system. ASAIO J 56:285–289. https://doi.org/10.1097/MAT.0b013e3181dfbab5
McKellar S (2020) A History of Mechanical Circulatory Support. In: Karimov J., Fukamachi K. SR (ed) Mechanical Support for Heart Failure. Springer, pp 3–17
Menter FR (1993) Zonal two equation k-w turbulence models for aerodynamic flows. AIAA
Mosterd A, Hoes AW (2007) Clinical epidemiology of heart failure. Heart 93:1137–1146. https://doi.org/10.1136/hrt.2003.025270
Pope SB (2001) Turbulent Flows. Cambridge University Press
Rezaienia MA, Paul G, Avital E, et al (2018) Computational parametric study of the axial and radial clearances in a centrifugal rotary blood pump. ASAIO J 64:643–650. https://doi.org/10.1097/MAT.0000000000000700
Schöps M, Groß-Hardt SH, Schmitz-Rode T, et al (2021) Hemolysis at low blood flow rates: in-vitro and in-silico evaluation of a centrifugal blood pump. J Transl Med 19:1–10. https://doi.org/10.1186/s12967-020-02599-z
Siemens CD-Adapco. STAR-CCM+ release version 15.02.007
Smith WA, Allaire P, Antaki J, et al (2004) Collected nondimensional performance of rotary dynamic blood pumps. ASAIO J 50:25–32. https://doi.org/10.1097/01.MAT.0000104817.39941.9C
Song X, Throckmorton AL, Wood HG, et al (2003) Computational fluid dynamics prediction of blood damage in a centrifugal pump. Artif Organs 27:938–941. https://doi.org/10.1046/j.1525-1594.2003.00026.x
Spiegel M, Redel T, Zhang JJ, et al (2011) Tetrahedral vs. polyhedral mesh size evaluation on flow velocity and wall shear stress for cerebral hemodynamic simulation. Comput Methods Biomech Biomed Engin 14:9–22. https://doi.org/10.1080/10255842.2010.518565
Stehlik J, Edwards LB, Kucheryavaya AY, et al (2010) The registry of the international society for heart and lung transplantation: twenty-seventh official adult heart

transplant report. J Hear Lung Transplant 29:1089–1103. https://doi.org/10.1016/j.healun.2010.08.007
Taskin ME, Fraser KH, Zhang T, et al (2012) Evaluation of Eulerian and Lagrangian models for hemolysis estimation. ASAIO J 58:363–372. https://doi.org/10.1097/MAT.0b013e318254833b
Thamsen B, Blümel B, Schaller J, et al (2015) Numerical analysis of blood damage potential of the HeartMate II and HeartWare HVAD rotary blood pumps. Artif Organs 39:651–659. https://doi.org/10.1111/aor.12542
Thamsen B, Gülan U, Wiegmann L, et al (2020) Assessment of the flow field in the HeartMate 3 using three-dimensional particle tracking velocimetry and comparison to computational fluid dynamics. ASAIO J 66:173–182. https://doi.org/10.1097/MAT.0000000000000987
Torregrosa AJ, Gil A, Quintero P, Tiseira A (2019) Enhanced design methodology of a low power stall regulated wind turbine. BEMT and MRF-RANS combination and comparison with existing designs. J Wind Eng Ind Aerodyn 190:230–244. https://doi.org/10.1016/j.jweia.2019.04.019
Wang Y, Shen P, Zheng M, et al (2019) Influence of impeller speed patterns on hemodynamic characteristics and hemolysis of the blood pump. Appl Sci 9:. https://doi.org/10.3390/app9214689
Wiegmann L, Boës S, de Zélicourt D, et al (2018) Blood pump design variations and their influence on hydraulic performance and indicators of hemocompatibility. Ann Biomed Eng 46:417–428. https://doi.org/10.1007/s10439-017-1951-0
Wiegmann L, Thamsen B, de Zélicourt D, et al (2019) Fluid dynamics in the HeartMate 3: influence of the artificial pulse feature and residual cardiac pulsation. Artif Organs 43:363–376. https://doi.org/10.1111/aor.13346
World Health Organization (2014) Global status report on noncommunicable diseases
Wu P, Huo J, Dai W, et al (2021) On the Optimization of a Centrifugal Maglev Blood Pump Through Design Variations. Front Physiol 12:1–10. https://doi.org/10.3389/fphys.2021.699891
Zhang J, Chen Z, Griffith BP, Wu ZJ (2020) Computational characterization of flow and blood damage potential of the new maglev CH-VAD pump versus the HVAD and HeartMate II pumps. Int J Artif Organs 43:653–662. https://doi.org/10.1177/0391398820903734